Journal of Materials Chemistry A

PAPER

View Article Online
View Journal

Cite this: DOI: 10.1039/c5ta08898d

WO_3 with surface oxygen vacancies as an anode buffer layer for high performance polymer solar cells†

Meng Qiu,[a] Dangqiang Zhu,[a] Xichang Bao,*[a] Junyi Wang,[a] Xuefei Wang*[b] and Renqiang Yang*[ac]

The exploration of inexpensive and efficient anode buffer layers is essential in large scale commercial applications of polymer solar cells (PSCs). Here, we report a simple way that can significantly enhance the power conversion efficiency (PCE) and extend the lifetime of PSCs. A solution-based tungsten oxide (WO_3) layer with surface oxygen vacancies (V_Os) is introduced as an efficient anode buffer layer between the active layer and indium tin oxide (ITO) glass. The PCEs of PSCs based on P3HT:$PC_{61}BM$ and PBDTTT–C:$PC_{71}BM$ active layers are improved by 24% (from 3.84% to 4.76%) and 27% (from 5.91% to 7.50%) with the introduction of the WO_3 (V_O) anode buffer layer, respectively, compared to that of the conventional PEDOT:PSS layer. The excellent performance is ascribed to the greatly improved fill factor and enhanced short circuit current density of the devices, which are benefited from the surface with lots of V_Os for better interfacial contact and excellent charge transport properties of the WO_3 (V_O) layer. The impressive PCE, good stability, easy fabrication and compatibility with solution processed organic photovoltaic devices support this material's potential applications in PSCs for both wide bandgap and narrow bandgap polymers.

Received 4th November 2015
Accepted 25th November 2015

DOI: 10.1039/c5ta08898d

www.rsc.org/MaterialsA

Introduction

Intensive effort has been devoted to the development of polymer solar cells (PSCs) in recent years due to their great potential in terms of low-cost, light weight, and easy fabrication on large-area flexible substrates.[1] Encouraging advances have been made, and state-of-the-art PSCs have reached efficiencies exceeding 10%.[2–4] However, much attention has been focused on the molecular structures and morphology of materials.[5–11] Challenges still exist in finding satisfactory anode buffer layers with reliable, environmentally robust and easily processable crafts. For conventional PSCs with indium tin oxide (ITO) as the anode, polyethylenedioxythiophene:polystyrenesulfonate (PEDOT:PSS) has been widely used as the anode buffer layer due to the higher work function as well as smoothening of the rough ITO film.[12,13] Unfortunately, the strong acidic nature of PEDOT:PSS causes inhomogeneous corrosion that deteriorates the electrical properties and degrades the stability of the cells.[14–18] To overcome this problem, a series of transition metal oxides, such as molybdenum oxide (MoO_3),[19,20] vanadium oxide (V_2O_5),[21–23] nickel oxide (NiO),[24–27] tungsten oxide (WO_3)[28–30] and rhenium oxide (ReO_3),[31] have been developed as alternative intermediate materials for the suitable work functions and air stability. These materials have been employed as hole injection layers in organic light-emitting diodes (OLEDs) and PSCs to reduce the injection barrier at the polymer/electrode interfaces.[32–34] Among those transition metal oxides, WO_3 is an extraordinary anode buffer layer for use in PSCs due to its suitable optical and electrical properties, high work function, air stability, low toxicity and capability of minimizing the series resistance and improving the fill factor of PSCs.[35–38] Generally, the preparation of WO_3 buffer layers in both OLEDs and PSCs is usually based on high-cost vacuum-based techniques, such as thermal evaporation, electron-beam evaporation, or hot filament vapor deposition.[39–50] Recently, solution-based methods have been used to fabricate WO_3 buffer layers,[51] but a post-annealing process is required to allow the precursors to thermally decompose into WO_3. In addition, the efficiency of state-of-the-art WO_3 buffer layer based cells is very limited,[30] because of the low conductivity and mediocre interfacial charge transfer of WO_3. Therefore, it seems greatly vital to improve the performance of the WO_3 buffer layer that is fabricated *via* low-cost solution-processed PSCs.

As is well known, even a very small decrease in the oxygen content gives rise to a dramatic increase in the electrical

[a]CAS Key Laboratory of Bio-based Materials, Qingdao Institute of Bioenergy and Bioprocess Technology, Chinese Academy of Sciences, Qingdao 266101, China. E-mail: baoxc@qibebt.ac.cn; yangrq@qibebt.ac.cn

[b]University of Chinese Academy of Sciences, Beijing 100049, China. E-mail: wangxf@ucas.ac.cn

[c]State Key Laboratory of Luminescent Materials and Devices, South China University of Technology, Guangzhou 510641, China

† Electronic supplementary information (ESI) available. See DOI: 10.1039/c5ta08898d

conductivity of WO_3.[52,53] A later study indicated that V_Os depending on oxygen pressure and temperature during the process of oxide film formation will greatly affect the film crystal structure, conductivity and charge transport properties. Through investigating the effect of V_Os on WO_3 conductivity, Gillet *et al.* realized that the defect band caused by V_Os increases the conductivity by lessening the band gap.[54] Liao *et al.* found that the O/W ratio and the amount of W^{6+} ions in the WO_3 nanowire films could be increased by increasing the annealing temperature, and the conductivity was decreased due to the reduced V_O concentration.[55] In the scope of photoelectricity, Li *et al.* fabricated WO_3 nanoflakes with V_Os by a simultaneous solution etching and reducing process, and found that the improved photoelectric conversion efficiency was attributed to the increased charge carrier density created by V_Os.[56] Cheng *et al.* introduced V_Os into commercial WO_3 *via* hydrogen treatment, and found the dual effect of V_Os that could serve as shallow electron donors to facilitate the charge migration and act as the active sites for absorbing electrolytes.[57] Therefore, one strategy to increase the conductivity of WO_3 and the interfacial charge transfer is to increase the V_O concentration appropriately.

Here, in order to improve the interfacial properties and simplify the preparation process of WO_3, an O_2 plasma process was introduced by replacing thermal annealing. A smooth WO_3 layer was prepared by spin coating tungsten(VI) isopropoxide propanol solution (5%) and then treated with O_2 plasma. The precursor can be decomposed to WO_3 by O_2 plasma directly. Most of all, the surface contains a large quantity of V_Os, which could not only increase the conductivity of WO_3 to facilitate the hole transfer, but also form excellent interfacial contact. Hence, the short circuit current density (J_{SC}) and fill factor (FF) were significantly increased when using WO_3 (V_O) as the anode buffer layer in PSCs. In this work, taking PEDOT:PSS, thermally annealed WO_3 (Δ) and O_2 plasma treated WO_3 (V_O) as the anode buffer layer independently, the photovoltaic performance of PSCs was investigated based on P3HT:PC_{61}BM (wide bandgap polymer) and PBDTTT–C:PC_{71}BM (narrow bandgap polymer). The PCE was improved by 24% (from 3.84% to 4.76%) and 27% (from 5.91% to 7.50%) with the introduction of the WO_3 (V_O) anode buffer layer, respectively, compared to that of PEDOT:PSS.

Results and discussion

The structure of the solution-based WO_3 layer was subjected to X-ray diffraction (XRD) measurements, as shown in Fig. 1(A). The broad diffraction peak at 2θ of 15–30° indicates the amorphous structure of the WO_3 layer, which is less rigid and shows a better tolerance to the interfacial contact than its crystalline counterpart. The transmittance spectra of the WO_3 layer on the ITO in comparison with those of the bare ITO substrate and the PEDOT:PSS layer on ITO are shown in Fig. 1(B). The high optical transmittance in the range of 330–430 nm was thought to be attributed to the smoothness of the ITO thin film surface with the PEDOT:PSS modification layer, which reduces dispersion and extinction of light caused by a rough surface (see the AFM section), which is in accordance with previous studies.[58] The WO_3 layer is highly transparent in the visible range and the transmittance of the samples coated with WO_3 prepared with different methods shows almost the same spectra, which is even better than the PEDOT:PSS layer in the wavelength range of 430–550 nm. X-ray photoelectron spectroscopy (XPS) measurements were taken to determine the purity and composition of the prepared WO_3 anode buffer layers, as shown in Fig. 2. The WO_3 films were fabricated through spin coating tungsten(VI) isopropoxide propanol solution (5%) at 4000 rpm on the pre-cleaned silicon substrate and then treated as the devices were prepared. The binding energies (BEs) are corrected with C 1s (284.42 eV). As shown in Fig. 2(A) and (B), the characteristic peaks of W, O and C elements in the 0–1200 eV BE range can be seen. The peaks having binding energies at 35.9, 38 and 42 eV correspond to W $4f_{7/2}$, W $4f_{5/2}$ and W $5p_{3/2}$, respectively, in WO_3 (+6 oxidation state, W^{6+}).[59,60] However, a careful study showed that the peaks at 34.5 and 36.6 eV corresponding to W $4f_{7/2}$ and W $4f_{5/2}$ of W^{5+} verify the existence of surface V_Os.[61,62] The peak with a binding energy of 530.5 eV is assigned to the oxygen atoms in WO_3, the peak at 531.5 eV is attributed to O atoms in sub-stoichiometric WO_x, and the peak at 532.5 eV is assigned to O in water molecules adsorbed on the surface of the film.[63] The XPS results demonstrate the presence of V_Os in the WO_3 film, generated from the reduction of W^{6+} to W^{5+} during the process of O_2 plasma treatment, which probably form defects and active sites for organic molecule bonding and facilitate interfacial charge transfer.

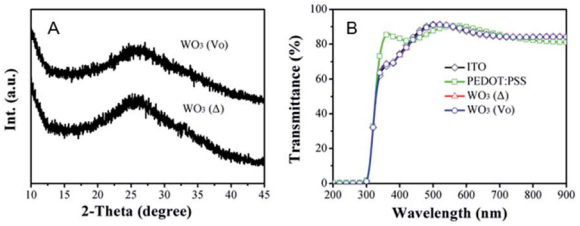

Fig. 1 1(A) X-ray diffraction (XRD) patterns of the WO_3 (Δ) and WO_3 (V_O) thin films on a silicon substrate, (B) optical transmittance of bare ITO coated glass, PEDOT:PSS, WO_3 (Δ) and WO_3 (V_O) layer modified ITO coated glass.

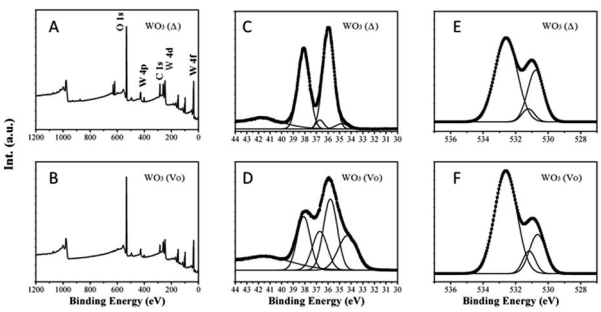

Fig. 2 XPS spectra of WO_3 (Δ) and WO_3 (V_O): (A and B) survey scan, (C and D) W 4f, and W 5p spectra and (E and F) O spectra of WO_3 (Δ) and WO_3 (V_O).

Surface morphologies of the WO_3 layers were investigated by tapping-mode atomic force microscopy (AFM). As shown in Fig. 3, compared to bare ITO with a roughness of 3.93 nm (Fig. 3(A)), the modification of the WO_3 layer under thermal annealing results in a lower roughness of 3.20 nm (Fig. 3(C)), which is still larger than that of PEDOT:PSS (2.31 nm) (Fig. 3(B)). While the O_2 plasma treated WO_3 (V_O) shows the lowest roughness of 1.59 nm (Fig. 3(D)), the decreased roughness of the surface is favorable for the interfacial contact. The surface energy of the WO_3 layer was explored by contact angle measurements as shown in Fig. 3 (E, F, G). The contact angle for the PEDOT:PSS layer is 17.41°, for the WO_3 (Δ) layer, it is increased to 34.17°, and interestingly, for WO_3 (V_O) it is 16.59°. The results show that the WO_3 (V_O) exhibited better interfacial affinity properties when the active layer was spin-coated onto it.

The PSCs with the structure of glass/ITO/WO_3/polymer:PCBM/Ca/Al, as shown in Fig. 4(A), were fabricated. Here, P3HT and PBDTTT–C were used as donors, as shown in Fig. 4(B), as well as $PC_{61}BM$ and $PC_{71}BM$ were used as acceptors. A schematic energy level diagram of the device is illustrated in Fig. 4(C). The energy levels are suitable for the charge separation and transport. Six types of devices as mentioned in the experimental section were prepared to investigate the effect of the WO_3 anode buffer layer on the performance of the PSCs. *J–V* curves of devices A–F under the illumination of AM 1.5 G, 100 mW cm^{-2} are shown in Fig. 5(A) and (B). The optimized device performance is summarized in Table 1. For P3HT:$PC_{61}BM$ based devices, device A with the traditional PEDOT:PSS anode buffer layer has a PCE of 3.84% with an open circuit voltage (V_{OC}) of 0.61 V, a short-circuit current density (J_{SC}) of 9.53 mA cm^{-2}, and a filled factor (FF) of 65.92%, comparable to that reported in the literature.[64] Device B with the WO_3 (Δ) anode layer shows a PCE of 4.23% with a V_{OC} of 0.62 V, a J_{SC} of 10.44 mA cm^{-2}, and a FF of 65.60%, which is consistent with WO_3 as the anode buffer layer prepared with tungsten isopropanol oxide reported previously.[30] In comparison, the PCE of device C with WO_3 (V_O) increases to 4.76%, with a higher J_{SC} and FF of 11.23 mA cm^{-2} and 68.14%, respectively. To further explore the generality of the WO_3 anode buffer layer in PSCs, another typical low bandgap donor polymer, PBDTTT–C, was studied.

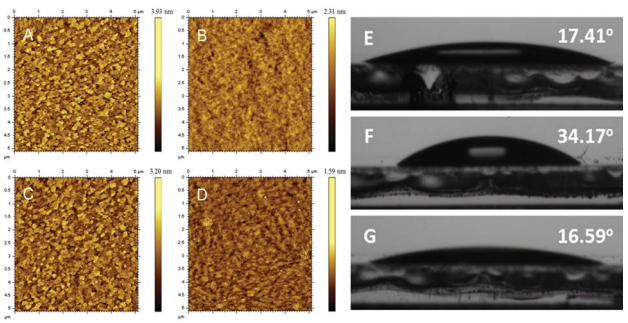

Fig. 3 AFM height images of (A) bare ITO-coated glass, (B) the control PEDOT:PSS layer, (C) the WO_3 (Δ) layer, (D) the WO_3 (V_O) layer. The scan size is 5 μm × 5 μm. Measured water contact angle between a droplet of deionized water and the anode buffer layer, (E) PEDOT:PSS, (F) WO_3 (Δ) and (G) WO_3 (V_O), respectively.

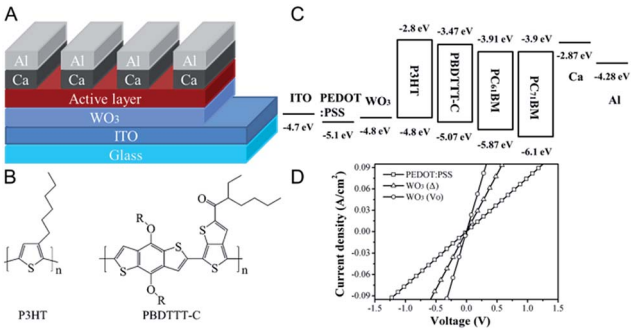

Fig. 4 (A) Device architecture and (B) molecular structures of polymers P3HT and PBDTTT–C. (C) Energy level diagram of materials investigated in this work. (D) Current–voltage characteristics of different anode buffer layers.

The *J–V* curves of the PSCs based on PBDTTT–C–T:$PC_{71}BM$ are shown in Fig. 5(B) and the related parameters are listed in Table 1. The traditional control device D with PEDOT:PSS as the anode buffer layer shows a PCE of 5.91% with a V_{OC} of 0.70 V, a J_{SC} of 15.54 mA cm^{-2}, and a FF of 54.21%. Another control device E with the WO_3 (Δ) anode buffer layer shows a PCE of 6.19% with a V_{OC} of 0.70 V, a J_{SC} of 15.27 mA cm^{-2}, and a FF of 57.19%. In contrast, device F with the WO_3 (V_O) anode buffer layer has a champion PCE of 7.50% with a V_{OC} of 0.70 V, a J_{SC} of 17.08 mA cm^{-2}, and a FF of 63.01%. *J–V* curves of devices C and F under various O_2 plasma processing times are shown in Fig. S1,† along with related parameters listed in Table S1.†

Meanwhile, the external quantum efficiencies (EQEs) of the solar cells with different anode buffer layers were also measured, as shown in Fig. 5(C and D). Compared to the device fabricated with PEDOT:PSS, the device fabricated with WO_3 (V_O) exhibited a higher EQE covering a wider spectral range. In particular for P3HT:$PC_{61}BM$ solar cells, the maximal EQE

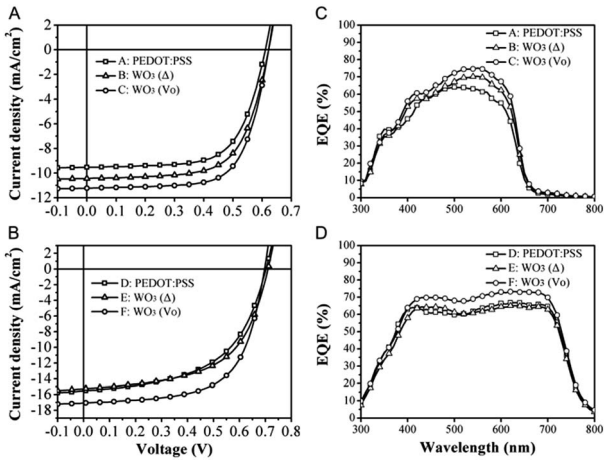

Fig. 5 *J–V* curves of the PSCs with different anode buffer layers responsible for the active layers of (A) P3HT:$PC_{61}BM$ and (B) PBDTTT–C:$PC_{71}BM$, respectively. EQE curves of the PSCs with different anode buffer layers responsible for the active layers of (C) P3HT:$PC_{61}BM$ and (D) PBDTTT–C:$PC_{71}BM$, respectively, under the illumination of AM 1.5 G, 100 mW cm^{-2}.

Table 1 Device parameters of the PSCs with different anode layers and active layers under the illumination of AM 1.5 G, 100 mW cm^{-2}

Device	V_{OC} (V)	J_{SC} (mA cm^{-2})	FF (%)	PCE (%)	R_S[a] (Ω cm^{-2})	Calcd J_{SC} (mA cm^{-2})
A	0.61	9.53	65.92	3.84	9.93	9.01
B	0.62	10.44	65.60	4.23	9.35	9.88
C	0.62	11.23	68.14	4.76	7.89	10.63
D	0.70	15.54	54.21	5.91	10.59	14.76
E	0.70	15.27	57.19	6.19	9.70	14.49
F	0.70	17.08	63.01	7.50	7.01	16.24

[a] Series resistance derived from *J–V* curves.

reached 75.03% at 550 nm for the device with a WO_3 (V_O) anode buffer layer, and showed a much better photoresponse in the broad range of 400–620 nm. While for PBDTTT–C:$PC_{71}BM$ solar cells, the maximal EQE reached 72.88% at 660 nm for the device with a WO_3 (V_O) anode buffer layer, and showed a much better photo response in the broad range of 400–720 nm. Moreover, the J_{SC} values calculated by integrating the EQE curves agree well with the J_{SC} values obtained from the *J–V* curves, as shown in Table 1. Combinedly, these account for a ~20% and 10% increase in the J_{SC} of P3HT and PBDTTT–C-based solar cells, respectively, indicating that the WO_3 (V_O) anode buffer layer was beneficial for device performance.

The resistance of the anode buffer layer is an important parameter that affects charge carrier transport and collection at the electrode. As shown in Fig. 4(D), the *J–V* curve of the WO_3 (V_O) layer exhibits the highest slope, *i.e.* the smallest resistance (4.0 Ω), while the PEDOT:PSS layer shows the lowest slope which means the largest resistance (13.4 Ω), and WO_3 (Δ) falls in between the both, with a mediate resistance (6.2 Ω). The better conductivity of WO_3 (V_O) is beneficial for carrier transport in the anode buffer layer. Moreover, the interfacial conductivity between the anode buffer layer and the active layer could guarantee efficient carrier transport from the polymer film to the WO_3 buffer layer. The series resistances (R_S) are listed in Table 1, revealing a descending trend from PEDOT:PSS, WO_3 (Δ) to WO_3 (V_O).

The interfacial charge transfer is a competitive process with exciton annealing, which results in photoluminescence (PL), therefore, time-correlated single-photon counting (TCSPC) was used to monitor the PL decay of the polymer films on various anode buffer layers to further confirm the charge transfer characteristics. The films of P3HT or PBDTTT–C on WO_3 buffer layers which have been annealed or treated by plasma O_2 were investigated, and for comparison, bare P3HT or PBDTTT–C films on glass were also measured. Unfortunately, we did not detect the PL from PBDTTT–C films due to the weak signal. For the data of P3HT, optimum fits were obtained for a single exponential function after convolution with the instrument response (Fig. 6). As is shown, the WO_3 (V_O) results in a slight decrease in the PL lifetime in comparison to the both cases of PEDOT:PSS and WO_3 (Δ). As we know, the PL of the active layer is arisen from the recombination of the excitons, which are generated by light excitation, and efficient interfacial charge transfer will accelerate the deactivation of the excitons thus resulting in fast PL decay.[65,66] The results indicate that the charge transfer process taking place at the interface of the polymer and WO_3 (V_O) is higher than that of PEDOT:PSS and WO_3 (Δ), which is consistent with the J_{SC} increase.

To obtain a deeper insight into the role of V_Os on the WO_3 surface, a slab model is employed to simulate the surface structures, and density functional theory (DFT) is used to investigate the electronic structure properties. V_Os are created by removing one (25% coverage) or two O atoms (50% coverage) on the clean (001) surface (0% coverage). Fig. 7A–C show the geometrical structure of WO_3 under various V_O coverages, and the corresponding band structures of (001) surfaces are also given in Fig. 7D–F. Evidently, the conduction bands tend to merge with the valence bands upon increasing V_O coverage. The decreased band gaps, from 1.28 eV to 0.99 eV, induced by V_Os lead to lower activation energy for the electron transition to increase the charge carrier density, which will increase the interfacial charge transfer and the conductivity of WO_3. This is in accordance with the experimental results.

The stability of photovoltaic devices with P3HT as the active layer and various anode buffer layers of PEDOT:PSS, WO_3 (Δ) and WO_3 (V_O) is investigated and represented in Fig. 8. The fast decay of PEDOT:PSS in all cases indicates its lower stability. The PCE decreases to less than 50% of the original value after 100 h

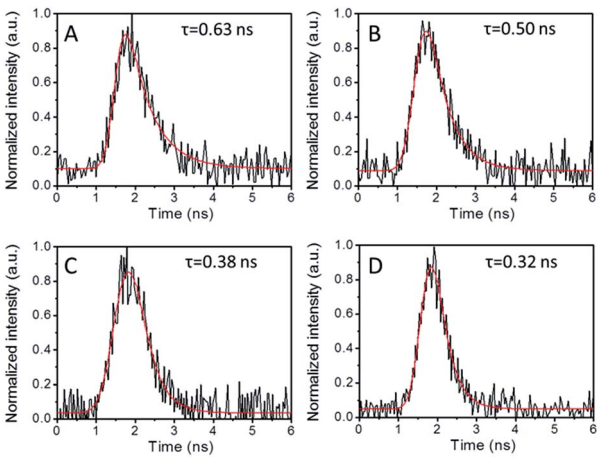

Fig. 6 The photoluminescence lifetime spectra of the pristine P3HT film (A) and P3HT on PEDOT:PSS (B), WO_3 (Δ) (C) and WO_3 (V_O) (D) layers, respectively.

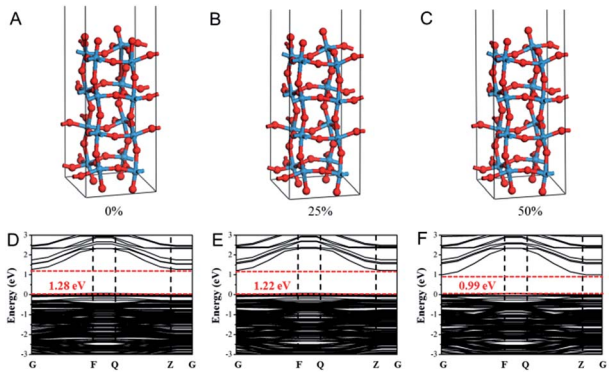

Fig. 7 The slab models and corresponding calculated band structures of the WO_3 surface with (A), (D) O termination, (B), (E) V_Os with a coverage of 25%, (C), (F) V_Os with a coverage of 50%.

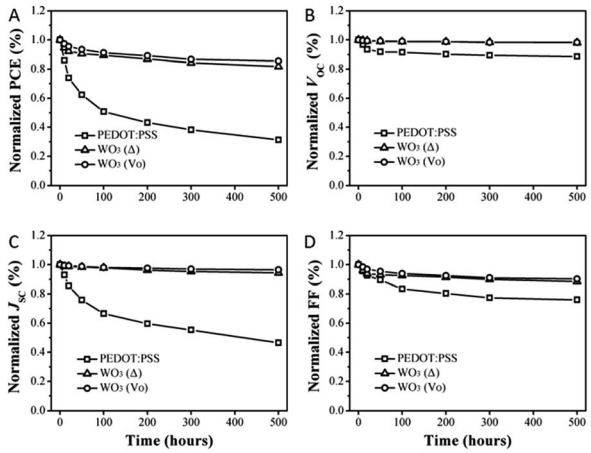

Fig. 8 Degradation of normalized (A) power conversion efficiency (PCE), (B) open circuit voltage (V_{OC}), (C) short circuit current density (J_{SC}), and (D) fill factor (FF) values of P3HT:$PC_{61}BM$ based PSC devices with different anode buffer layers of PEDOT:PSS, WO_3 (Δ) and WO_3 (V_O), respectively.

exposure in a glovebox, and less than 40% after 500 h. The decrease is mainly ascribed to the obvious decay in both J_{SC} and FF. The stability of PSCs is improved dramatically with the introduction of WO_3 anode buffer layers between the active layer and the anode ITO. The PCE retains above 80% of its initial value after 500 h. The J_{SC} and FF of PSCs with the WO_3 buffer layer drop more slowly than that with the PEDOT:PSS buffer layer. The J_{SC} shows negligible reduction over time (Fig. 8(C)), which could be attributed to the stable nature of WO_3. The stability evaluation of devices with PBDTTT–C as the active layer and various anode buffer layers of PEDOT:PSS, WO_3 (Δ) and WO_3 (V_O) exhibits a similar trend (Fig. S2†).

Conclusions

In summary, we demonstrate efficient polymer solar cells (PSCs) using solution-processed annealing free WO_3 anode buffer layers prepared by spin-coating a tungsten oxide alcohol solution on the ITO electrode and then treating by O_2 plasma. The WO_3 layer shows high light transmittance, high conductivity, and enhanced interfacial charge transfer. The PSCs with the WO_3 (V_O) anode buffer layer exhibit improved performance in comparison with conventional PEDOT:PSS and annealed WO_3 anode buffer layers. The higher performance of the device is ascribed to the modified surface with lots of V_Os for better interfacial contact and excellent electrical transport properties. DFT calculation further confirms that the band gaps of WO_3 decrease with increased V_O concentration to lower the activation energy for the electron transition, which is beneficial for the interfacial charge transfer and the conductivity of WO_3. The PSCs presented here are far from being fully optimized, but the profound advantages along with ease of preparation, good stability and applicability for potential cost-effective manufacturing processes make it a good candidate for the anode buffer layer in PSCs. This work provides insights into the design of the interfacial hole transport layer for the fabrication of PSCs. The obtained results are therefore very encouraging and expected to be a new strategy to enhance the photovoltaic performance of PSCs.

Experimental

Materials and preparation

ITO coated glass with a sheet resistance of 15 Ω sq^{-1} was supplied by Shenzhen Display Co, Ltd (China). Tungsten(VI) isopropoxide (5% w/v in isopropanol) was purchased from Alfa Aesar. P3HT and PBDTTT–C were bought from Lumtec and Solarmer, respectively. $PC_{61}BM$ and $PC_{71}BM$ were purchased from American Dye Sources (ADS). 1,8-Diiodooctane (DIO) was obtained from Sigma Aldrich. All commercially available materials were used directly without any further purification.

Device fabrication

Six types of PSCs are designed as follows:

(A) ITO/PEDOT:PSS (30 nm)/P3HT:$PC_{61}BM$ (200 nm)/Ca (10 nm)/Al (100 nm), (B) ITO/WO_3 (Δ, 16 nm)/P3HT:$PC_{61}BM$ (200 nm)/Ca (10 nm)/Al (100 nm), (C) ITO/WO_3 (V_O, 16 nm)/P3HT:$PC_{61}BM$ (200 nm)/Ca (10 nm)/Al (100 nm), (D) ITO/PEDOT:PSS (30 nm)/PBDTTT–C:$PC_{71}BM$ (90 nm)/Ca (10 nm)/Al (100 nm), (E) ITO/WO_3 (Δ, 16 nm)/PBDTTT–C:$PC_{71}BM$ (90 nm)/Ca (10 nm)/Al (100 nm), and (F) ITO/WO_3 (V_O, 16 nm)/PBDTTT–C:$PC_{71}BM$ (90 nm)/Ca (10 nm)/Al (100 nm).

The ITO coated glass was sequentially ultrasonically washed in detergent, deionized water, acetone, and isopropanol for 20 min each time. Then the pre-cleaned ITO coated glass was exposed to oxygen plasma to remove organic contaminants and increase the wetting envelope. PEDOT:PSS aqueous solution was spin-coated at 4000 rpm for 20 s on ITO coated glass, and then baked at 150 °C for 30 min in air. The WO_3 was prepared by spin coating tungsten(VI) isopropoxide propanol solution (5%) at 4000 rpm on pre-cleaned ITO coated glass, and then annealed at 150 °C for 10 min in air (WO_3 (Δ)) or treated under O_2 plasma (WO_3 (V_O)) for 9 min. Subsequently, the modified ITO coated glass was transferred to the glovebox filled with N_2 and the

active layer was prepared by spincoating the blend solution of donor materials and fullerene derivatives quickly. For P3HT:$PC_{61}BM$ based devices, the active layer was prepared by using the dichlorobenzene solution of P3HT and $PC_{61}BM$ (1 : 1 w/w, polymer concentration of 18 mg mL^{-1}) on the modified ITO electrode, and then thermally annealed at 150 °C for 10 min on a hot plate. The thickness of the active layer was around 200 nm. For PBDTTT–C:$PC_{71}BM$ based devices, the active layer was prepared by spin-coating the dichlorobenzene solution of PBDTTT-C and $PC_{71}BM$ (1 : 1.5 w/w, polymer concentration of 12.5 mg mL^{-1}) with 3% volume ratio of the DIO additive on the modified ITO electrode. The thickness of the photoactive layer was about 90 nm. Finally, the substrate was transferred to a vacuum chamber and a Ca (10 nm)/Al (100 nm) bilayer cathode electrode was thermally deposited on the active layer under a base pressure of 4×10^{-4} Pa. The photoactive area of the device was 0.1 cm^2 which is defined by a shadow mask.

Characterization and measurements

The grazing incidence X-ray diffraction (GIXRD) pattern was obtained on a Bruker D8 ADVANCE. The X-ray photoelectron spectroscopy (XPS) results were obtained with an ESCA Lab250i-XL electron spectrometer from Thermo using 150 W Al Kα radiation. The transmission spectra of the films on ITO coated glass were recorded by using a scanning spectrophotometer (Varian Cary 50 UV-vis) in the range of 250–800 nm at room temperature. Surface morphological characterization studies of the films were characterized by using a tapping-mode atomic force microscope (AFM, Agilent 5400). The water contact angle measurements were carried out on a JY-82 contact angle system (China). Deionized water is obtained from a Millipore ultrapure water system. Current density–voltage (*J–V*) characteristics of the devices were measured with a Keithley 2420 source measurement unit under the illumination of AM 1.5 G, 100 mW cm^{-2} with a Newport solar simulator. The light intensity was calibrated with a standard silicon solar cell. The external quantum efficiencies (EQE) of solar cells were analyzed using a certified Newport incident photon conversion efficiency (IPCE) measurement system. The TCSPC was performed using a home-built setup equipped with a picosecond pulsed laser (P-C-405B, 400 nm, 50 ps) and a photomultiplier (PMA-C-182 M).

Ab initio calculation

Periodic density functional theory (DFT) calculations were performed using the Vienna *Ab initio* simulation package (VASP).[67,68] Ultrasoft pseudo-potential and generalized gradient approximation (GGA) parameterized with the Perdew–Burke–Ernzerhof (PBE) exchange–correlation functional were adopted.[69] The electron–ion interaction was described by the projector-augmented wave (PAW) scheme.[70,71] In the slab model, the (001) surface of γ-monoclinic WO_3 with the space group of *P*21/*n* was considered, for it's the most stable surface at room temperature. The first two atom layers were allowed to relax, the bottom layers of the slab were fixed. And the vacuum region was set to 15 Å between atom layers. A ($3 \times 3 \times 1$) Monkhorst–Pack scheme *k*-points sampling was used.[72] During the process of structure optimization, the convergence criteria for energy, force and max displacement were set to be 10^{-5} eV, 0.03 eV $Å^{-1}$ and 1.0×10^{-3} Å, respectively. The cutoff energy for the plane-wave expansion was 400 eV.

Acknowledgements

This work was supported by the Ministry of Science and Technology of China (2014CB643501, 2010DFA52310), and the National Natural Science Foundation of China (21274161, 51173199, 51573205, 61107090 and 91233107).

Notes and references

1 C. J. Brabec, S. Gowrisanker, J. J. M. Halls, D. Laird, S. Jia and S. P. Williams, *Adv. Mater.*, 2010, **22**, 3839.
2 J. You, L. Dou, K. Yoshimura, T. Kato, K. Ohya, T. Moriarty, K. Emery, C. Chen, J. Gao, G. Li and Y. Yang, *Nat. Commun.*, 2013, **4**, 1446.
3 S. Liao, H. Jhuo, P. Yeh, Y. Cheng, Y. Li, Y. Lee, S. Sharma and S. Chen, *Sci. Rep.*, 2014, **4**, 6813.
4 Y. Liu, J. Zhao, Z. Li, C. Mu, W. Ma, H. Hu, K. Jiang, H. Lin, H. Ade and H. Yan, *Nat. Commun.*, 2014, **5**, 5293.
5 Y. Huang, E. J. Kramer, A. J. Heeger and G. C. Bazan, *Chem. Rev.*, 2014, **114**, 7006.
6 A. C. Stuart, J. R. Tumbleston, H. Zhou, W. Li, S. Liu, H. Ade and W. You, *J. Am. Chem. Soc.*, 2013, **135**, 1806.
7 J. Kim, C. E. Song, I. Kang, W. S. Shin and D. Hwang, *Chem. Commun.*, 2013, **49**, 3248.
8 T. Lei, J. Wang and J. Pei, *Acc. Chem. Res.*, 2014, **47**, 1117.
9 P. C. Chow, S. Albert Seifried, S. Gélinas and R. H. Friend, *Adv. Mater.*, 2014, **26**, 4851.
10 J. Wu, S. Cheng, Y. Cheng and C. Hsu, *Chem. Soc. Rev.*, 2015, **44**, 1113.
11 Y. Huang, E. J. Kramer, A. J. Heeger and G. C. Bazan, *Chem. Rev.*, 2014, **114**, 7006.
12 H. Frohne, S. E. Shaheen, C. J. Brabec, D. C. Muller, N. S. Sariciftci and K. Meerholz, *ChemPhysChem.*, 2002, **3**, 795.
13 H. Park, R. M. Howden, M. C. Barr, V. Bulovic, K. Gleason and J. Kong, *ACS Nano*, 2012, **6**, 6370.
14 F. So and D. Kondakov, *Adv. Mater.*, 2010, **22**, 3762.
15 K. Norrman, S. A. Gevorgyan and F. C. Krebs, *ACS Appl. Mater. Interfaces*, 2009, **1**, 102.
16 M. Jorgensen, K. Norrman and F. C. Krebs, *Sol. Energy Mater. Sol. Cells*, 2008, **92**, 686.
17 C. Ionescu-Zanetti, A. Mechler, S. A. Carter and R. Lal, *Adv. Mater.*, 2004, **16**, 385.
18 M. P. de Jong, L. J. van IJzendoorn and M. J. A. de Voigt, *Appl. Phys. Lett.*, 2000, **77**, 2255.
19 K. Zilberberg, H. Gharbi, A. Behrendt, S. Trost and T. Riedl, *ACS Appl. Mater. Interfaces*, 2012, **4**, 1164.
20 H. Schmidt, H. Fluegge, T. Winkler, T. Buelow, T. Riedl and W. Kowalsky, *Appl. Phys. Lett.*, 2009, **94**, 243302.
21 C. Chen, Y. Chen and S. Chuang, *Adv. Mater.*, 2011, **23**, 3859.
22 L. Shen, S. Ruan, W. Guo, F. Meng and W. Chen, *Sol. Energy Mater. Sol. Cells*, 2012, **97**, 59.

23 L. Shen, Y. Xu, F. Meng, F. Li, S. Ruan and W. Chen, *Org. Electron.*, 2011, **12**, 1223.
24 W. Yu, L. Shen, F. Meng, Y. Long, S. Ruan and W. Chen, *Sol. Energy Mater Sol. Cells*, 2012, **100**, 226.
25 F. Li, S. Ruan, Y. Xu, F. Meng, J. Wang, W. Chen and L. Shen, *Sol. Energy Mater Sol. Cells*, 2011, **95**, 877.
26 K. X. Steirer, P. F. Ndione, N. E. Widjonarko, M. T. Lloyd, J. Meyer, E. L. Ratcliff, A. Kahn, N. R. Armstrong, C. J. Curtis, D. S. Ginley, J. J. Berry and D. C. Olson, *Adv. Energy Mater*, 2011, **1**, 813.
27 M. D. Irwin, B. Buchholz, A. W. Hains, R. P. H. Chang and T. J. Marks, *Proc. Natl. Acad. Sci. U. S. A.*, 2008, **105**, 2783.
28 T. Stubhan, N. Li, N. A. Luechinger, S. C. Halim, G. J. Matt and C. J. Brabec, *Adv. Energy Mater.*, 2012, **2**, 1433.
29 C. Tao, S. Ruan, G. Xie, X. Kong, L. Shen, F. Meng, C. Liu, X. Zhang, W. Dong and W. Chen, *Appl. Phys. Lett.*, 2009, **94**, 043311.
30 Z. Tan, L. Li, C. Cui, Y. Ding, Q. Xu, S. Li, D. Qian and Y. Li, *J. Phys. Chem. C*, 2012, **116**, 18626.
31 D. Kim, T. Kim, W. Jeong and J. Kim, *Appl. Phys. Lett.*, 2012, **101**, 153303.
32 S. Y. Ryu, J. H. Noh, B. H. Hwang, C. S. Kim, S. J. Jo, J. T. Kim, H. S. Hwang, H. K. Baik, H. S. Jeong, C. H. Lee, S. Y. Song, S. H. Choi and S. Y. Park, *Appl. Phys. Lett.*, 2008, **92**, 023306.
33 J. Meyer, S. Hamwi, T. Buelow, H. H. Johannes, T. Riedl and W. Kowalsky, *Appl. Phys. Lett.*, 2007, **91**, 113506.
34 J. Z. Li, M. Yahiro, K. Ishida, H. Yamada and K. Matsushige, *Synth. Met.*, 2005, **151**, 141.
35 M. Y. Chan, C. S. Lee, S. L. Lai, M. K. Fung, F. L. Wong, H. Y. Sun, K. M. Lau and S. T. Lee, *J. Appl. Phys.*, 2006, **100**, 094506.
36 S. Han, W. S. Shin, M. Seo, D. Gupta, S. Moon and S. Yoo, *Org. Electron.*, 2009, **10**, 791.
37 A. G. F. Janssen, T. Riedl, S. Hamwi, H. H. Johannes and W. Kowalsky, *Appl. Phys. Lett.*, 2007, **91**, 073519.
38 M. Vasilopoulou, L. C. Palilis, D. G. Georgiadou, P. Argitis, S. Kennou, I. Kostis, G. Papadimitropoulos, N. A. Stathopoulos, A. A. Iliadis, N. Konofaos, D. Davazoglou and L. Sygellou, *Thin Solid Films*, 2011, **519**, 5748.
39 S. Y. Ryu, J. H. Noh, B. H. Hwang, C. S. Kim, S. J. Jo, J. T. Kim, H. S. Hwang, H. K. Baik, H. S. Jeong, C. H. Lee, S. Y. Song, S. H. Choi and S. Y. Park, *Appl. Phys. Lett.*, 2008, **92**, 023306.
40 J. Z. Li, M. Yahiro, K. Ishida, H. Yamada and K. Matsushige, *Synth. Met.*, 2005, **151**, 141.
41 M. Vasilopoulou, L. C. Palilis, D. G. Georgiadou, P. Argitis, S. Kennou, I. Kostis, G. Papadimitropoulos, N. A. Stathopoulos, A. A. Iliadis, N. Konofaos, D. Davazoglou and L. Sygellou, *Thin Solid Films*, 2011, **519**, 5748.
42 C. Tao, G. Xie, F. Meng, S. Ruan and W. Chen, *J. Phys. Chem. C*, 2011, **115**, 12611.
43 S. Han, W. S. Shin, M. Seo, D. Gupta, S. Moon and S. Yoo, *Org. Electron.*, 2009, **10**, 791.
44 C. Tao, G. Xie, C. Liu, X. Zhang, W. Dong, F. Meng, X. Kong, L. Shen, S. Ruan and W. Chen, *Appl. Phys. Lett.*, 2009, **95**, 0533035.
45 C. Tao, S. Ruan, G. Xie, X. Kong, L. Shen, F. Meng, C. Liu, X. Zhang, W. Dong and W. Chen, *Appl. Phys. Lett.*, 2009, **94**, 0433114.
46 J. Meyer, S. Hamwi, T. Buelow, H. H. Johannes, T. Riedl and W. Kowalsky, *Appl. Phys. Lett.*, 2007, **91**, 11350611.
47 A. G. F. Janssen, T. Riedl, S. Hamwi, H. H. Johannes and W. Kowalsky, *Appl. Phys. Lett.*, 2007, **91**, 0735197.
48 M. Y. Chan, C. S. Lee, S. L. Lai, M. K. Fung, F. L. Wong, H. Y. Sun, K. M. Lau and S. T. Lee, *J. Appl. Phys.*, 2006, **100**, 0945069.
49 G. Leftheriotis, S. Papaefthimiou and P. Yianoulis, *Sol. Energy Mater. Sol. Cells*, 2004, **83**, 115–124.
50 A. Rougier, F. Portemer, A. Quede and M. El Marssi, *Appl. Surf. Sci.*, 1999, **153**, 1.
51 L. Chen, C. Xie and Y. Chen, *Adv. Funct. Mater.*, 2014, **24**, 3986–3995.
52 V. O. Makarov and M. Trontelj, *J. Eur. Ceram. Soc.*, 1996, **16**, 791.
53 W. Sahle and M. Nygren, *J. Solid State Chem.*, 1983, **48**, 154.
54 M. Gillet, C. Lemire, E. Gillet and K. Aguir, *Surf. Sci.*, 2003, **532**, 519.
55 C. Liao, F. Chen and J. Kai, *Sol. Energy Mater. Sol. Cells*, 2007, **91**, 1258.
56 W. Li, P. Da, Y. Zhang, Y. Wang, X. Lin, X. Gong and G. Zheng, *ACS Nano*, 2014, **8**, 11770.
57 L. Cheng, Y. Hou, B. Zhang, S. Yang, J. W. Guo, L. Wu and H. G. Yang, *Chem. Commun.*, 2013, **49**, 5945.
58 S. Na, G. Wang, S. Kim, T. Kim, S. Oh, B. Yu, T. Lee and D. Kim, *J. Mater. Chem.*, 2009, **19**, 9045.
59 G. Leftheriotis, S. Papaefthimiou, P. Yianoulis, A. Siokou and D. Kefalas, *Appl. Surf. Sci.*, 2003, **218**, 275.
60 G. Leftheriotis, S. Papaefthimiou, P. Yianoulis and A. Siokou, *Thin Solid Films*, 2001, **384**, 298.
61 A. Siokou, G. Leftheriotis, S. Papaefthimiou and P. Yianoulis, *Surf. Sci.*, 2001, **482**, 294.
62 O. Anderson and K. Bange, *Fresenius' J. Anal. Chem.*, 1991, **341**, 74.
63 H. Y. Wong, C. W. Ong, R. Kwok, K. W. Wong, S. P. Wong and W. Y. Cheung, *Thin Solid Films*, 2000, **376**, 131.
64 W. L. Ma, C. Y. Yang, X. Gong, K. Lee and A. J. Heeger, *Adv. Funct. Mater.*, 2005, **15**, 1617.
65 S. D. Stranks, G. E. Eperon, G. Grancini, C. Menelaou, M. J. Alcocer, T. Leijtens, L. M. Herz, A. Petrozza and H. J. Snaith, *Science*, 2013, **342**, 341.
66 G. Xing, N. Mathews, S. Sun, S. S. Lim, Y. M. Lam, M. Grätzel, S. Mhaisalkar and T. C. Sum, *Science*, 2013, **342**, 344.
67 G. Kresse and J. Furthmüller, *Comput. Mater. Sci.*, 1996, **6**, 15.
68 G. Kresse and J. Furthmüller, *Phys. Rev. B*, 1996, **54**, 11169.
69 J. P. Perdew, K. Burke and M. Ernzerhof, *Phys. Rev. Lett.*, 1996, **77**, 3865.
70 P. E. Blöchl, *Phys. Rev. B*, 1994, **50**, 17953.
71 G. Kresse and D. Joubert, *Phys. Rev. B*, 1999, **59**, 1758.
72 H. J. Monkhorst and J. D. Pack, *Phys. Rev. B*, 1976, **13**, 5188.